Acta Mechanica Sinica
DOI

RESEARCH PAPER

A numerical study on wind-driven runback characteristics of a thin water film flow over a solid surface

Jincheng Wang, Ping He, and Hui Hu*

Department of Aerospace Engineering, Iowa State University, Ames, IA 50011, USA

Abstract

An unsteady numerical simulation is conducted to examine the dynamic runback characteristics of a water film flow driven by a boundary layer airflow over a solid surface pertinent to the dynamic glaze ice accretion process over aircraft wing surfaces. The multiphase flow simulation results of the wind-driven water runback (WDWR) flow are compared quantitatively with the experimental results in terms of the time-dependent variations of the water film thickness profiles and evolution of the front contact point (FCP) of the runback water film flow. The underlying mechanism of the intermittent water runback behavior is elucidated by analyzing the time evolution of the airflow velocity and vorticity fields above the runback water film flow over the solid surface. To the best knowledge of the authors, the work presented here is the first successful attempt to numerically examine the transient runback characteristics of WDWR flows. It serves as an excellent benchmark case for the development of best practices to model the important micro-physical processes responsible for the transient water transport over aircraft wing surfaces.

Keywords Multiphase flow simulation; Water transport over wing surfaces; Glaze ice accretion process; Volume of fluid method.

1 Introduction

Ice accumulation on aircraft surfaces presents a critical safety concern with substantial impacts on the aerodynamic performance of aircraft through increased aerodynamic drag, decreased lift generation, and reduced stall angles. The ice formation occurs when supercooled water droplets in the clouds encounter the frontal surfaces of aircraft at specific temperature conditions, leading to immediate freezing upon contact [1–9]. Under glaze icing conditions, characterized by high liquid water content (LWC) and large supercooled droplets, only a portion of the supercooled water droplets would freeze instantly upon impact, while the rest of the impinged supercooled water droplets would stay in the liquid phase. The unfrozen water droplets would coalesce rapidly to form thin water films, which would flow freely over the airframe surfaces as driven by boundary layer airflows [10–15]. The wind-driven runback of the unfrozen water plays a crucial role in the overall ice formation process through both direct and indirect mechanisms, as its kinetic properties significantly influence how the supercooled water droplets disperse upon contact with airframe surfaces [16–21]. Hansman and Turnock [10] demonstrated that wind-driven runback water flow affected the final shape of glaze ice formations substantially. A subsequent study by Waldman and Hu [22] revealed how the stagnation characteristics of wind-driven water runback flows influenced ice formation patterns on the surface of an airfoil/wing model.

Significant advances have been made recently in simulating/modeling wind-driven water runback flows pertinent to aircraft icing phenomena. A groundbreaking work was conducted by Matheis and Rothmayer [23], who employed lubrication theory to simulate surface waves on thin water films, revealing that these waves could enhance film mass flux by up to 50%. Building on this work, Wang and Rothmayer [24] developed a lubrication theory-based model to analyze thin water film transport across small-scale surface roughness. Their model successfully reproduced well-known phenomena in surface water transportation, including water pooling between roughness elements. Further developments came from Lan et al. [25], who utilized the volume of fluid (VOF) method to simulate wind-driven thin film flow under turbulent airflow conditions. Their research demonstrated the importance of incorporating dynamic contact angle modeling for accurate prediction of surface water transport. In parallel with the efforts to understand steady-state characteristics, Dong et al. [26] and Lou et al. [27] advanced the field by developing rivulet models for simulating steady-state runback water film flows over airfoil surfaces. These models provided reliable estimates of both film thickness

* Corresponding author. E-mail address: huhui@iastate.edu

and rivulet width. Most recently, Jordan et al. [28] conducted a direct numerical simulation of wind-driven thin film flow over airfoil surfaces. Their study yielded valuable insights into the interactions between liquid films and free-stream airflow, particularly regarding unsteady film thickness and natural waviness generation.

It should be noted that the transient nature of the WDWR flows has been largely overlooked in previous numerical studies, primarily due to two significant challenges. The first is the technical difficulty in experimental studies to obtain spatially-and-temporally-resolved measurements to quantify transient characteristics of wind-driven water film/rivulet flows for the verification/validation of numerical simulations. The second challenge lies in the complexity of numerical modeling, as matching the transient state of a wind-driven water runback (WDWR) flow between unsteady numerical simulations and time-dependent experimental measurements require extensive parametric studies, unlike simplified comparisons of time-averaged quantities of wind-driven water film/rivulet flows.

This study presents a multiphase flow simulation to investigate the transient runback characteristics of a wind-driven water film/rivulet flow over a solid surface. The multiphase flow simulation is validated/verified quantitively against time-resolved experimental measurements in terms of the time-dependent variations of the water film thickness profiles and evolution of the front contact point (FCP) of the WDWR flow over the solid surface. To the best knowledge of the authors, the work presented here is the first successful endeavor to model the transient runback characteristics of WDWR flows which are compared quantitatively with the spatially-and-temporally-resolved experimental results obtained by using a novel Digital Image Projection (DIP) technique [29]. The good agreement between the unsteady multiphase flow simulation and time-resolved DIP measurements serves as an outstanding benchmark for the development of rigorous methods to model wind-driven water transport processes over solid surfaces, leading to more accurate modeling and prediction of complex glaze ice accretion process over aircraft wing surfaces.

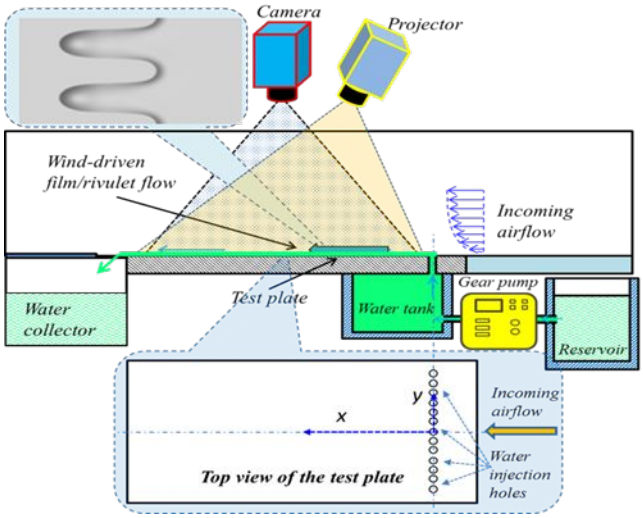

Figure 1. Experimental setup used to quantify transient runback characteristics of wind-driven water film flows [29].

2 Experiment setup and measurement results.

The experimental results reported by Zhang and Hu [29] are used to validate/verify the multiphase flow simulation of the present study. Figure 1 shows schematically the experimental setup used in the experimental study to quantify the characteristics of the transient WDWR flows over a test plate [29]. While a flat test plate was flush mounted on the bottom wall of the test section of a low-speed wind tunnel, de-ionized water was pumped from a reserve tank through an array of small holes spanning 60 mm in width (i.e., D = 60 mm), at the front of the test plate. An advanced DIP system was used to achieve spatially-and-temporally-resolved measurements of the water film thickness distributions of the wind-driven water runback flow over the test plate. The DIP system covered an observation area of 100 mm (i.e., streamwise direction) by 60 mm (i.e., spanwise direction) with the digital camera for DIP image acquisition at the frame rate of 30.0 frames per second, capturing 200 snapshots per test condition. Two key parameters were controlled during the experiments: 1). the freestream speed (V_∞) of the incoming airflow, and 2). the flow rate of the water film (Q). As the first step of a comprehensive multiphase flow simulation to examine transient runback characteristics of wind-driven water film/rivulet flows under various flow conditions pertinent to complex aircraft icing phenomena, the work reported here considers a simple, quasi-3D WDWR condition only, where the freestream speed of the incoming airflow was maintained at a relatively low speed of V_∞ = 10 m/s, and the water film flow rate was set at Q = 100 ml/min. The representative results of the DIP

measurements at three nondimensional time moments (i.e., t^* = 0.25, t^* = 0.50, and t^* = 1.0) are given in Fig. 2, where $t^* = t / t_{end}$ with t_{end} = 4.3 seconds is the duration that the front contact of the WDWR flow reaching to the downstream location of x/D = 1.0. The FCP refers to the utmost downstream location of the front contact line of the WDWR flow.

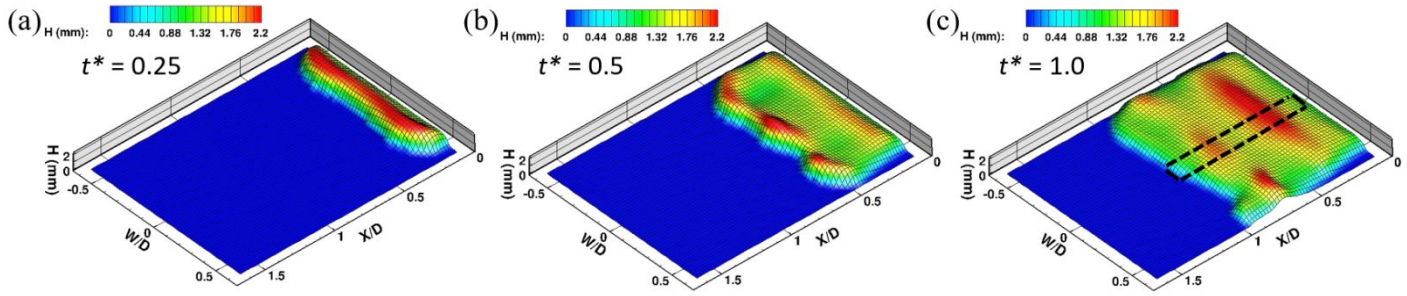

Figure 2. Representative DIP measurement results of the WDWR flow with V_∞ = 10 m/s and Q = 100 ml/min. The dashed region in Fig. 2(c) demonstrates the region from which the water film thickness profiles are extracted and averaged for the experiment data given in Section 4. H denotes water film thickness, W denotes spanwise location, and x denotes streamwise location.

3 Numerical model

3.1. OpenFOAM.

The multiphase flow simulation of the present study utilizes the interFOAM solver from the OpenFOAM v2206 software package, which implements the finite volume method and the VOF methodology for analyzing two-phase, incompressible flows. Further information about the implementation and methodology of the solver is available in the reference [30].

In general, the flow is governed by the mass and momentum conversation equations:

$$\nabla \cdot \mathbf{U} = 0, \tag{1}$$

$$\frac{\partial}{\partial t}(\rho \mathbf{U}) + \nabla(\rho \mathbf{U}\mathbf{U}) = -\nabla p + \nabla[2\mu \mathbf{S} - \frac{2}{3}\mu(\nabla \mathbf{U})\mathbf{I}] + \rho \mathbf{f}_b, \tag{2}$$

where $\mathbf{S}$ is the mean rate of strain tensor $0.5[\nabla \mathbf{U} + (\nabla \mathbf{U})^T]$ and $\mathbf{f}_b$ is the body forces.

The VOF methodology employs a single effective flow velocity while distinguishing between two-phase fluids through a fractional parameter β, which ranges from 0 to 1. The air phase and water phases are represented by $\beta = 0$ and $\beta = 1$, respectively. A cell containing $\beta = 0.5$ indicates an equal volumetric distribution of both fluids. The fluid density ρ, viscosity μ, and velocity $\mathbf{U}$ are determined as a function of this fraction variable β and the respective properties of the constituent fluids:

$$\rho = \beta \rho_a + (1-\beta)\rho_w \tag{3}$$

$$\mu = \beta \mu_a + (1-\beta)\mu_w \tag{4}$$

$$\mathbf{U} = \beta \mathbf{U}_a + (1-\beta)\mathbf{U}_w \tag{5}$$

where subscript a represents air phase and subscript w represents the water phase.

The transport equation for fraction variable β is derived from a two-fluid Eulerian model [30]:

$$\frac{\partial \beta}{\partial t} + \nabla(\mathbf{U}\beta) + \nabla\left[(\mathbf{U}_w - \mathbf{U}_a)\beta(1-\beta)\right] = 0 \tag{6}$$

where the third term is zero inside a single species but sharpens the interface between two fluids. This formulation removes the need for specialized convection schemes.

3.2. Initial conditions and boundary conditions.

As revealed by the experimental studies of Liu et al. [31] and Zhang and Hu [29], wind-driven water film flows over flat surfaces were featured with the generation of well-organized, two-dimensional (2D) surface waves at the water/air interface under the test conditions with relatively low wind speed and small water flowrate. Therefore, 2D multiphase flow simulation was conducted in the present study with the computational domain shown in Fig. 3, where the third dimension, i.e., the spanwise direction, is D = 60 mm.

For boundary conditions of phase fraction β, the airflow inlet (left wall) has a fixed value of 0, while the water inlet has a fixed value of 1. A dynamic contact angle model [32] is applied to the bottom wall:

$$\theta_{dyn} = \theta_{static} + (\theta_{adv} - \theta_{rec}) \tanh(u_w / u_\theta), \quad (7)$$

where θ_{dyn} is the dynamic contact angle, θ_{static} is the static contact angle, θ_{adv} is the advancing contact angle, θ_{rec} is the receding contact angle, u_w is the interface velocity parallel to the bottom wall, and u_θ is the characteristic velocity for the contact line. Based on the information provided in the reference [29], the above parameters are set as follows: $\theta_{static} = 65°$, $\theta_{adv} = 80°$, $\theta_{rec} = 10°$, and $u_\theta = 0.014$ m/s. For the top and right walls, the phase fraction boundary conditions are zero gradients.

For velocity boundary conditions of the airflow, a boundary layer velocity profile measured by using a digital Particle Image Velocimetry (PIV) system [29] is applied to the airflow inlet to align with the velocity distribution of the experiment, where the freestream velocity of the airflow is V_∞ = 10 m/s, and the boundary layer thickness is 2.8 mm. The velocity profile measured by PIV was proved to agree with the Blasius solution, so the airflow is laminar. For the water flow inlet, given the width of the water hole array of D = 60 mm and the diameter of the water hole of 2 mm, the velocity of water flow at the inlet is set to be 0.014 m/s to satisfy the water flow rate constraint, which is Q = 100 ml/min. The bottom wall is set to be nonslip. The top wall is set to be a slip boundary condition. The right wall is set to have zero gradient.

For initial conditions, the phase fraction β of the whole domain is set to be zero (air), except that the small 5 mm × 2 mm rectangular domain at the bottom (Fig. 3) is set to be 1 (water). The initial pressure field is set to be zero uniformly over the domain. The initial velocity field of the air phase over the entire domain is set to be the same as the boundary layer velocity profile of the air inlet, which means water is pumped out after the air flow is fully developed and stable.

3.3. Physical properties of the flows

To align the physical properties of the fluids in the numerical simulation with those in the experiments [14], the density of air and water is set to be 1.19 kg/m^3 and 998.2 kg/m^3, respectively. The kinetic viscosity of air and water are set to be v_a = 1.526 × 10^{-5} m^2/s and v_w =1.0034 × 10^{-6} m^2/s, respectively. The surface tension of water is set to be 0.072 N/m. The Reynolds number of the airflow above the water inlet is estimated to $Re_{inlet} = V_\infty \times X_{inlet}/v_a$ = 16,600, where X_{inlet} = 25.4 mm is the distance between the water inlet and the leading edge of the test plate used in the experimental study [29]. The Reynolds number of the airflow at the end of the computational domain is $Re_{end} = V_\infty \times X_{end}/v_a$ = 75,000, where X_{end} = 114.4 mm is the distance between the end of the computational domain and the leading edge of the flat plate used in the experimental study [29]. The Reynolds number of the water film/rivulet flow is $Re_w = Q/(D*v_w)$ = 27.7.

3.4. Mesh independence study.

For the computational domain shown in Fig. 3, the size of initial coarse uniform cartesian grid is 0.2 mm × 0.2 mm across the whole domain. For the domain within the green dashed rectangle (8 mm × 91 mm), as shown in Fig. 3, three different levels of grid refinement are tested for grid independence, i.e., 0.1 mm × 0.1 mm, 0.05 mm × 0.05 mm, and 0.025 mm × 0.025 mm. The marching speed of the FCP (i.e., the speed of the leading edge of the water film) simulated from the above four different grids are compared. The marching speeds of the above four cases are normalized by the marching speed of the case with the finest grid, as shown in Fig. 4. The horizontal axis indicates the number of overall mesh elements corresponding to cases with different refinement levels of mesh. It can be found that the marching speed converges as the grid size decreases to around 0.05 mm. As a result, the grid of 0.05 mm × 0.05 mm is utilized in the present study. The corresponding number of the mesh elements is 256,005.

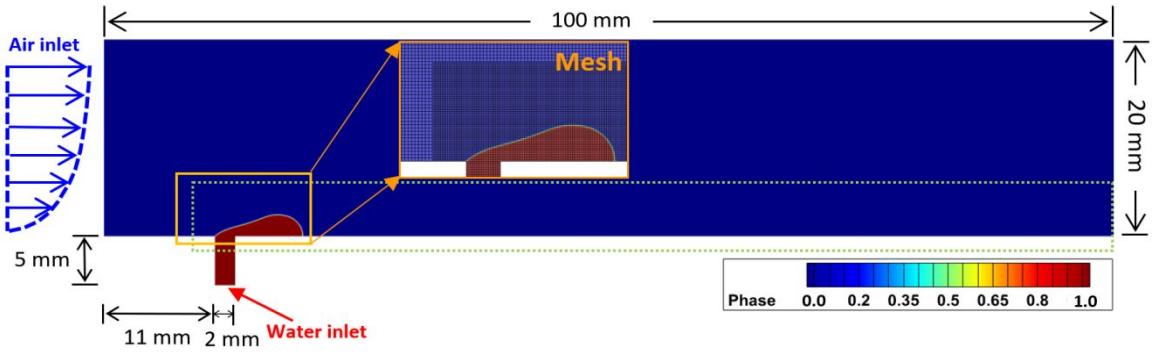

Figure 3. Computational domain for WDWR flow simulation. The mesh within the dashed-line rectangular region is refined with an example of the refined mesh around the water film being magnified in the subfigure.

The time step is automatically adjusted to make the maximum Courant number less than 1.0. The minimum time step is 3.0 $\times 10^{-7}$ s during the simulation. The total physical time for the numerical simulation is the same as the experiment duration. The wall clock run time for the case with 0.05 mm × 0.05 mm grids is about 64 hours with 36 cores of Intel Xeon Gold 6240 CPU.

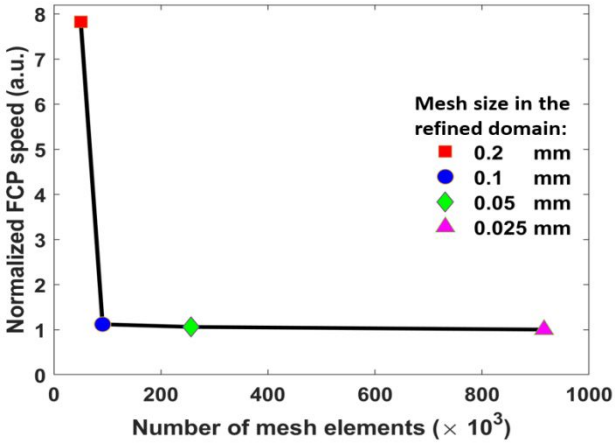

Figure 4 Grid independence test results based on the front contact point speed of WDWR flow. The speeds are normalized by the speed of the case with the finest mesh size.

4 Results and Discussions

4.1. Simulation results of the WDWR flow

Figure 5 gives typical multiphase flow simulation results of the WDWR flow under the condition of V_∞ = 10 m/s and Q = 100 ml/min. The 2D simulation results are extruded into 3D for a clear comparison to the measured film thickness distributions given in Fig. 2. The simulation results are selected to have the same nondimensional time as the experimental results (i.e., t^* = 0.25, t^* = 0.50, t^* = 0.75, t^* = 1.0). It can be seen clearly that, for the test cases with the freestream velocity of the airflow being relatively low (i.e., V_∞ = 10 m/s), rather well-organized, two-dimensional surface waves are found to be generated at the air/water interface of the WDWR flow over the test plate. The global features of the WDWR flow revealed from the multiphase flow simulation (i.e., the generation of well-organized, two-dimensional surface waves at the air/water interface) are found to agree well with the experimental observations reported by Liu et al. [31] and the DIP measurements given in Fig. 2. This agreement shows that the two-dimensional assumption for wind-driven water film structure holds under low wind Reynolds number.

It should be noted that the DIP measurements of Zhang and Hu [29] confirmed that the WDWR flow under this test condition would become three-dimensional after the frontal contact line of the WDWR flow reaching downstream locations of x/D > 1.0. Therefore, the multiphase flow simulation stops when the front contact line of the WDWR flow reaches x/D = 1.0 since the 2D assumption of the WDWR flow used for the multiphase flow simulation would not be valid anymore after that moment.

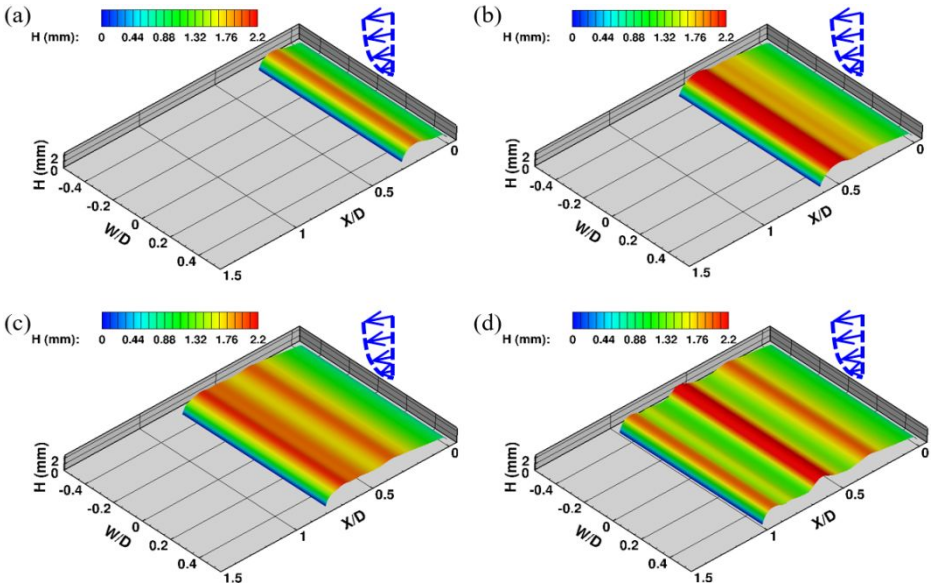

Figure 5. Representative simulation results of the WDWR flow at (a) t^*= 0.25, (b) t^* = 0.5, (c) t^* = 0.75, and (d) t^* = 1.0. The surface is obtained from the iso-surface of β = 0.25 and the surface color indicates the film thickness.

4.2. Comparison between numerical simulation and experimental measurement results

In the present study, the multiphase flow simulation of the WDWR flow is validated/verified quantitatively with the experimental results obtained under the same flow conditions [29]. Figure 6 shows the multiphase flow simulation results in terms of the water film thickness profiles of the WDWR flow over the test plate against the experiment results at the time instants of (a) t^*= 0.25, (b) t^* = 0.50, (c) t^* = 0.75, and (d) t^* = 1.00, respectively. The thickness profile of the simulation is extracted using the built-in "interfaceHeight" functional object in OpenFOAM, which is an integral approach that calculates the height of the two-phase interface above a set of user-specified locations. The experiment results given in the plot are extracted from the DIP measurement results given in Fig. 2, which are the spanwise-averaged water film thickness data near the midplane of the WDWR flow (i.e., within the 5.0 mm-wide region indicated by the dashed lines shown in Fig. 2c).

As shown clearly in Fig. 6, the morphology at the air/water interface of the simulated WDWR flow agrees well with that of the experimental results at all the compared time instants. It is also revealed clearly that the pressure and aerodynamic shear forces exerted by the incoming airflow would push the frontal contact line of the WDWR flow moving forward continuously at the beginning of the runback process. As the WDWR flow spreads rapidly over the test surface, well-organized surface waves are found to form at the air/water interface which dominates the dynamic runback behavior of the WDWR flow and water transport process over the test surface, as described in Liu et al. [31]. It should be noted that the differences in the mean water film thickness of the WDWR flow between the simulation and the experimental result are found to be within ±7.5 % over the entire computational time horizon, which is much smaller than the prediction errors (i.e., ≥ ± 20%) reported in the existing steady simulations of wind-driven runback water film/rivulet flows [27, 28]. The discrepancies between the simulation and the experiment results shown in Fig. 6 are believed to be closely associated with the difficulty in modeling the adhesive forces caused by the microstructures on surface of the test plate of the multiphase flow simulation to be exactly the same as that of the experiments. More advanced surface modeling to account for the adhesive force caused by the existence of the microstructures on the test surface is needed for more accurate simulation/prediction of the transient runback behavior of the WDWR flows.

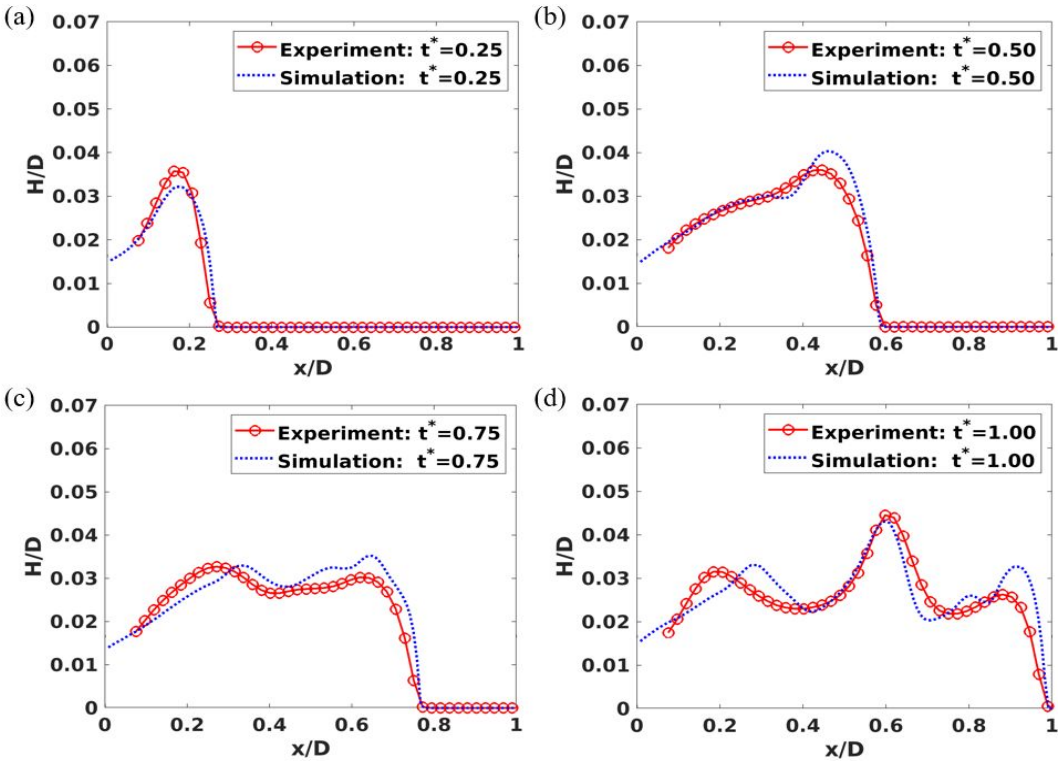

Figure 6. Comparison of the water film thickness of the WDWR flow on the test plate between the simulation and experimental results at the time instants of (a) t^*= 0.25, (b) t^* = 0.50, (c) t^* = 0.75, and (d) t^* = 1.00, respectively.

4.3. Comparison of the time evolution of the front contact point of the WDWR flow.

As reported in the experimental studies of Zhang and Hu [29] and Liu et al.[31], a general runback feature of WDWR flows is the stumbling motion of the water film heads in "start-and-stop" cycles. To better reveal dynamic stumbling runback feature of the WDWR flow, Fig. 7 gives the time evolution of the front contact point of the water film over the test plate derived from the multiphase flow simulation, which reveals the stumbling runback motion of the water film heads clearly and quantitively. The experimental results, which are extracted based on the time-resolved DIP measurements as those shown in Fig. 2, are also given in the plot for a quantitative comparison.

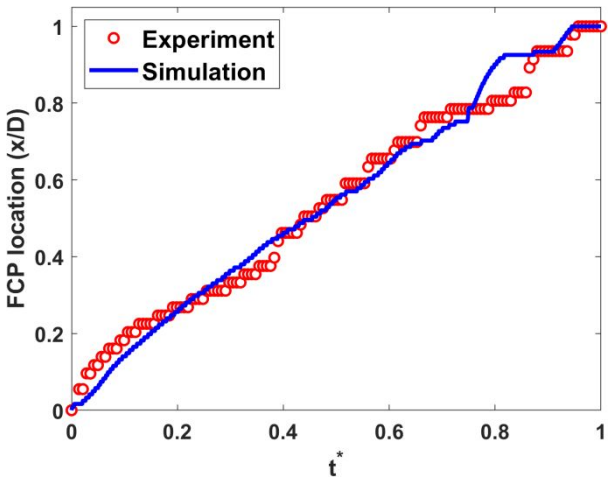

Figure 7. Comparison of the time evolution of the front contact point of the WDWR flow over the test surface between the multiphase flow simulation and experimental results.

To evaluate the performance of the simulation, a non-dimensional parameter, named as coefficient of determination of the runback water film front, is introduced to quantify how well the multiphase flow simulation of the WDWR flow agrees with the experiment results under the test condition used in the present study:

$$R = \sqrt{1 - \frac{\sum_{i=1}^{N}\left(F_i - \text{[illegible]}\right)^2}{\sum_{i=1}^{N}\left(\text{[illegible]} - \overline{F}\right)^2}}, \tag{8}$$

where F_i is the FCP location of the simulation at a certain time moment, [illegible] is the FCP location of the experiment at a certain time moment, N is the number of sampled FCP locations in the entire time horizon, and $\overline{F_i}$ is the average of N experimental FCP locations. The R value of 1.0 indicates a perfect agreement between the numerical predictions and the experimental results [33]. Based on the data points given in Fig. 7, the R value of the FCP locations between the numerical simulation and the experiment results is found to be 0.97, which demonstrates a very good agreement between the multiphase flow simulation of the transient behavior of the WDWR flow with the experimental measurements.

4.4. Insights into the underlying mechanism of the intermittent runback behavior of the WDWR flow

As shown in Fig. 7, the movement of the front contact point of the WDWR flow is a stumbling motion with obvious "start-and-stop" pattern in both the simulation and experimental results. This phenomenon occurs when the balance of the forces near the contact point is disrupted during the competition between surface tension, pressure force, and aerodynamic shear force. Based on the time-resolved DIP measurements of the WDWR flows under different test conditions, Zhang and Hu [29] suggested that the aerodynamic shear force would have the most significant effects on the stumbling runback behavior of WDWR flow. In this section, the detailed velocity and vorticity fields within the boundary layer airflow above the wind-driven water film flow over the test plate is examined carefully to elucidate the underlying mechanisms of the stumbling runback behavior of the WDWR flow. Such quantitative information about the transient runback behavior of the WDWR flow would be very difficult, if not impossible, to obtain via experimental measurements.

Figure 8 shows the typical multiphase flow simulation results in terms of the airflow velocity and vorticity fields over the WDWR flow during the breakoff of the stagnated water film head, which marks the restart of the water runback process. The velocity magnitude is normalized by the freestream velocity of the airflow, i.e., V_∞ = 10 m/s. From Figs. 8(a-c), it can be found that the boundary layer thickness is thickened due to the presence of the water film and the airflow velocity near the water film surface is much slower than the velocity of the freestream airflow. This large velocity gradient near the water film surface induces high interfacial shear stress on the free surface of the water film, which induces the formation of the surface waves. Since the interfacial shear stress is proportional to the velocity gradient of the airflow, the vorticity near the surface of the water film is a proper indicator to manifest the magnitude of the interfacial shear force exerted on the water film.

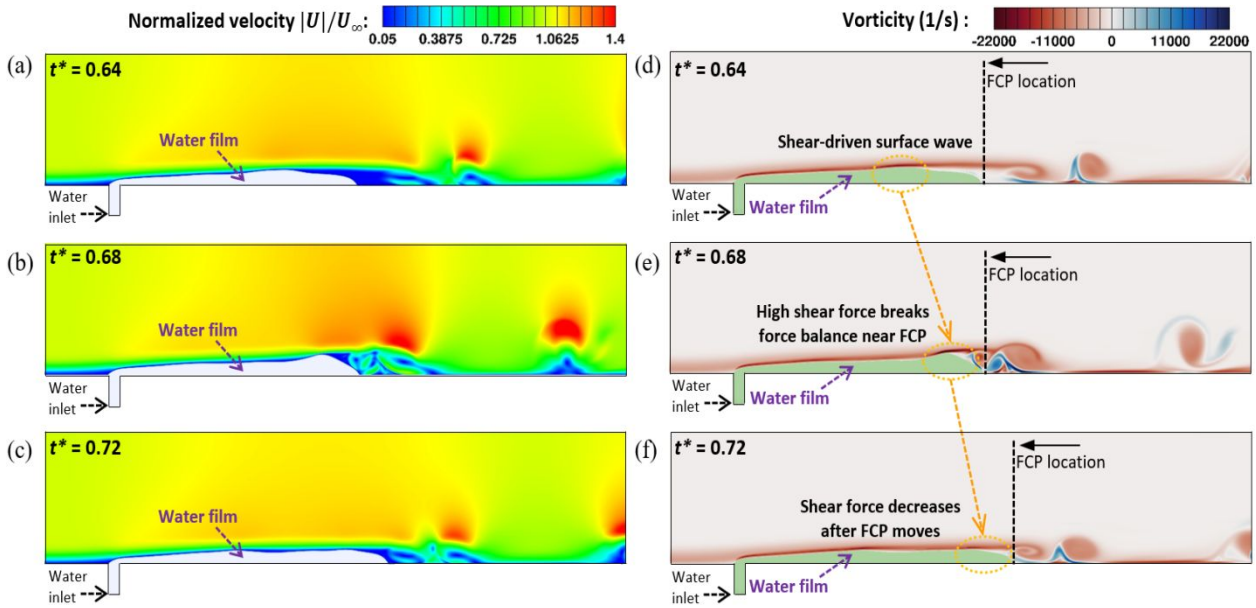

Figure 8. Typical simulation results of airflow velocity distributions (a-c) and vorticity fields(d-f) at three consecutive time instants to elucidate the underlying mechanism of the stumbling runback behavior of the WDWR flow.

The vorticity fields corresponding to the velocity fields in Figs. 8(a-c) are shown in Figs. 8(d-f). It can be found that vortices form and shed in the wake region of the runback water film. As indicated in Figs. 8(d)(e), the FCP location is not moving between $t^* = 0.64$ and $t^* = 0.68$, which is because the restraining surface tension force is stronger than the aerodynamic shear force near the FCP before $t^* = 0.68$.

However, at $t^* = 0.68$, the shear-driven surface wave at $t^* = 0.64$, marked by the dashed circle in Fig. 8(d), just moves from upstream to the proximity of FCP at $t^* = 0.68$ with increasing vorticity (i.e., interfacial shear force) near the crest of the surface wave. The higher shear force on the water surface is because of the increase in the height of the surface wave. In the context of a thin water film driven by a high-speed boundary layer airflow, the gradient of the velocity between the air speed and the water surface speed will increase as the water film increases [34]. Since the shear force is proportional to the velocity gradient, the interfacial shear force on the water surface increases as the water film thickness increases. Therefore, the force balance at the FCP will be destroyed by the presence of the surface wave driven by the higher shear force. As a result, the FCP is found to march downstream after $t^* = 0.68$.

As shown in Fig. 8(f), the FCP marches to further downstream at $t^* = 0.72$ but stops again because of the decreases in the interfacial shear force on the surface of the water head near FCP. Under the principle of mass conservation, when the wetted area of the water film expands, the thickness of the water film at the leading edge decreases immediately, resulting in reduced interfacial shear force. The above intermittent nature of the water runback behavior repeats throughout the entire wind-driven flow process, causing the stumbling motion of the water film head of the WDWR flow in "start-and-stop" cycles as observed in previous experimental studies [29, 31].

5 Conclusion

A numerical study with a VOF-based multiphase flow solver is conducted to examine the transient runback characteristics of a water film flow driven by a boundary layer airflow over a solid surface pertinent to dynamic glaze ice accretion process over aircraft wing surfaces. Rigorous quantitative validation of the computational multiphase flow simulation was achieved by quantitatively comparing with time-resolved experimental measurements to examine the evolution of water film thickness distributions and FCP as WDWR flow marches across the solid surface. While the results of the multiphase flow simulation are found to agree with the time-resolved experimental measurements well in general, important characteristics of the wind-driven water runback process, such as the generation of well-organized two-dimensional surface waves at the air/water interface, stumbling runback motion of the water film heads in "start-and-stop" cycles, are revealed clearly and quantitatively based on the unsteady numerical simulation results. The

underlying mechanism of the intermittent water runback behavior (i.e., stumbling motion of the water runback process in "start-and-stop" cycles), is elucidated by analyzing the transient velocity and vorticity fields of the multiphase simulation results.

For future research, the combination of the first principle-based multiphase flow simulation and machine learning-based WDWR flow predictions [33, 35, 36] would provide a promising path for more accurate modeling and prediction of aircraft icing phenomena to ensure safer and more efficient aircraft operation in cold climates.

Conflict of interest. On behalf of all authors, the corresponding author states that there is no conflict of interest

Author contributions. ***Jincheng Wang***: Conceptualization; Data curation; Formal analysis; Investigation; Methodology; Validation; Visualization; Writing–original draft. ***Ping He***: Conceptualization; Methodology; Validation; Visualization; Writing–review & editing. ***Hui Hu***: Conceptualization; Formal analysis; Funding acquisition; Investigation; Methodology; Project administration; Resources; Software; Supervision; Validation; Visualization; Writing–review& editing.

Acknowledgments The research was partially supported by the National Science Foundation (NSF) of USA under Award Numbers of TIP-2140489, CBET- 2313310, and CBET- 2415347.

References

1. Cao, Y., Tan, W., Wu, Z.: Aircraft icing: An ongoing threat to aviation safety. Aerosp Sci Technol. 75, 353–385 (2018). https://doi.org/https://doi.org/10.1016/j.ast.2017.12.028
2. Gent, R.W., Dart, N.P., Cansdale, J.T.: Aircraft icing. Philosophical Transactions of the Royal Society A: Mathematical, Physical and Engineering Sciences. 358, 2873–2911 (2000). https://doi.org/10.1098/RSTA.2000.0689
3. Bragg, M., Basar, T., Perkins, W., Selig, M., Voulgaris, P., Melody, J., Sarter, N.: Smart icing systems for aircraft icing safety. In: 40th AIAA Aerospace Sciences Meeting & Exhibit. American Institute of Aeronautics and Astronautics (2002)
4. Thomas, S.K., Cassoni, R.P., MacArthur, C.D.: Aircraft anti-icing and de-icing techniques and modeling. J Aircr. 33, 841–854 (1996). https://doi.org/10.2514/3.47027
5. Bragg, M.B., Gregorek, G.M., Lee, J.D.: Airfoil aerodynamics in icing conditions. J Aircr. 23, 76–81 (1986). https://doi.org/10.2514/3.45269
6. Anderson, D.N., Tsao, J.-C.: Overview of icing physics relevant to scaling. SAE transactions. 31–46 (2003)
7. Cao, Y., Yuan, K.: Aircraft flight characteristics in conditions of windshear and icing. The Aeronautical Journal. 111, 41–49 (2007). https://doi.org/DOI: 10.1017/S0001924000001743
8. Zheng, C., Jin, Z., Du, X., Dong, Q., Yang, Z.: Effects of simplified horn ice shapes on flow structures around an airfoil. Acta Mechanica Sinica. 40, 323344 (2024). https://doi.org/https://doi.org/10.1007/s10409-023-23344-x
9. Wang, Y., Zhang, Y., Wang, Y., Zhu, C., Zhao, N., Zhu, C.: Early warning and thickness measurement of aircraft icing using ultrasonic pulse echoes. Proc Inst Mech Eng G J Aerosp Eng. (2025). https://doi.org/10.1177/09544100251315880
10. Hansman, R.J., Turnock, S.R.: Investigation of surface water behavior during glaze ice accretion. J Aircr. 26, 140–147 (1989). https://doi.org/10.2514/3.45735
11. Politovich, M.K.: Predicting Glaze or Rime Ice Growth on Airfoils. J Aircr. 37, 117–121 (2000). https://doi.org/10.2514/2.2570
12. Yanxia, D., Yewei, G., Chunhua, X., Xian, Y.: Investigation on heat transfer characteristics of aircraft icing including runback water. Int J Heat Mass Transf. 53, 3702–3707 (2010). https://doi.org/10.1016/j.ijheatmasstransfer.2010.04.021
13. Da Silva, G.A.L., De Mattos Silvares, O., De Jesus Zerbiniz, E.J.G., Hefazi, H., Chen, H.H., Kaups, K.: Differential boundary-layer analysis and runback water flow model applied to flow around airfoils with thermal anti-ice. In: 1st AIAA Atmospheric and Space Environments Conference (2009)
14. Craik, A.D.D.: Wind-generated waves in thin liquid films. J Fluid Mech. 26, 369–392 (1966). https://doi.org/DOI: 10.1017/S0022112066001289
15. Phillips, O.M.: On the generation of waves by turbulent wind. J Fluid Mech. 2, 417–445 (1957). https://doi.org/DOI: 10.1017/S0022112057000233
16. Olsen, W.A., Walker, E.N.: Experimental evidence for modifying the current physical model for ice accretion on aircraft surfaces. Presented at the (1986)
17. Cober, S.G., Isaac, G.A.: Characterization of aircraft icing environments with Supercooled Large Drops for application to commercial aircraft certification. J Appl Meteorol Climatol. 51, 265–284 (2012). https://doi.org/10.1175/JAMC-D-11-022.1
18. Brahimi, M., Tran, P., Chocron, D., Tezok, F., Paraschivoiu, I.: Effect of supercooled large droplets on ice accretion characteristics. In: 35th Aerospace Sciences Meeting and Exhibit. American Institute of Aeronautics and Astronautics (1997)
19. Khojasteh, D., Kazerooni, M., Salarian, S., Kamali, R.: Droplet impact on superhydrophobic surfaces: A review of recent developments, (2016)
20. Tang, T., Jin, T., Wang, G.: Numerical study on dynamics of oblique hollow droplet impact on a liquid film. Acta Mechanica Sinica. 39, 323175 (2023). https://doi.org/https://doi.org/10.1007/s10409-023-23175-x

21. Jurman, L.A., McCready, M.J.: Study of waves on thin liquid films sheared by turbulent gas flows. Physics of Fluids A: Fluid Dynamics. 1, 522–536 (1989). https://doi.org/10.1063/1.857553
22. Waldman, R.M., Hu, H.: High-Speed Imaging to Quantify Transient Ice Accretion Process over an Airfoil. J Aircr. 53, 369–377 (2016). https://doi.org/10.2514/1.C033367
23. Matheis, B., Rothmayer, A.: Numerical simulation of thin air driven films. In: 40th AIAA Aerospace Sciences Meeting & Exhibit. American Institute of Aeronautics and Astronautics (2002)
24. Wang, G., Rothmayer, A.P.: Thin water films driven by air shear stress through roughness. Comput Fluids. 38, 235–246 (2009). https://doi.org/https://doi.org/10.1016/j.compfluid.2008.02.009
25. Lan, H., Friedrich, M., Armaly, B.F., Drallmeier, J.A.: Simulation and measurement of 3D shear-driven thin liquid film flow in a duct. Int J Heat Fluid Flow. 29, 449–459 (2008). https://doi.org/https://doi.org/10.1016/j.ijheatfluidflow.2007.12.003
26. Dong, W., Zheng, M., Zhu, J., Lei, G.: Calculation and Analysis of Runback Water Flow on Anti-Icing Airfoil Surface. J Aircr. 53, 1597–1605 (2016). https://doi.org/10.2514/1.C033637
27. Lou, Y., Bu, X., Shen, X., Lin, G., Zhang, R., Zeng, F., Jin, H., Ma, K., Wen, D.: Simulation of and Experimental Research on Rivulet Model on Airfoil Surface. Aerospace. 9, (2022). https://doi.org/10.3390/aerospace9100570
28. Sakakeeny, J.A., McClain, S.T., Ling, Y.: Direct Numerical Simulation of a Thin Film Over a NACA 0012 Airfoil. In: 2018 Atmospheric and Space Environments Conference. American Institute of Aeronautics and Astronautics (2018)
29. Zhang, K., Hu, H.: An experimental study on the transient runback characteristics of wind-driven film/rivulet flows. Physics of Fluids. 33, 112104 (2021). https://doi.org/10.1063/5.0067672
30. Berberović, E., van Hinsberg, N.P., Jakirlić, S., Roisman, I. V, Tropea, C.: Drop impact onto a liquid layer of finite thickness: Dynamics of the cavity evolution. Phys Rev E. 79, 36306 (2009). https://doi.org/10.1103/PhysRevE.79.036306
31. Liu, Y., Chen, W.-L., Bond, L.J., Hu, H.: An experimental study on the characteristics of wind-driven surface water film flows by using a multi-transducer ultrasonic pulse-echo technique. Physics of Fluids. 29, 12102 (2017). https://doi.org/10.1063/1.4973398
32. Hoffmann, A., Spiegel, S., Heckmann, T., Scharfer, P., Schabel, W.: CFD model of slot die coating for lithium-ion battery electrodes in 2D and 3D with load balanced dynamic mesh refinement enabled with a local-slip boundary condition in OpenFOAM. J Coat Technol Res. 20, 3–14 (2023). https://doi.org/10.1007/s11998-022-00660-8
33. Wang, J., Hu, H., He, P., Hu, H.: A machine learning study to predict wind-driven water runback characteristics. Physics of Fluids. 35, 102104 (2023). https://doi.org/10.1063/5.0167545
34. Wang, J., Chumbley, E., Hu, H.: An Experimental Study on Wind-Driven Flowoff Characteristics of Deicing Fluids Pertinent to Aircraft Ground Deicing. In: AIAA AVIATION FORUM AND ASCEND 2024. American Institute of Aeronautics and Astronautics (2024)
35. Wang, J., He, P., Hu, H.: Predicting Interfacial Shear Stress Distributions of Wind-Driven Water Runback Flows Using Physics-Informed Neural Networks. In: AIAA AVIATION FORUM AND ASCEND 2024. American Institute of Aeronautics and Astronautics (2024)
36. Wang, J., Hu, H., He, P., Hu, H.: A Data-Driven Approach to Study Nonlinear Dynamics of Wind-Driven Water Runback Flows Pertinent to Aircraft Icing Phenomena. In: AIAA AVIATION 2023 Forum. American Institute of Aeronautics and Astronautics (2023)